High Performance Flexible Visible-Blind UV Photodetectors with 2DEG based on Unconventional Release Strategy

Yi-Yu Zhang[1)], *Yi-Xiong Zheng*[2)], *Jun-Yu Lai*[2)], *Jung-Hun Seo*[2)], *Kwang Hong Lee*[3)], *Chuan Seng Tan*[1,3)], *Shu An*[1)], *Sang-Ho Shin*[1)], *Bongkwon Son*[1)], *and Munho Kim*[1),*]

[1)]School of Electrical and Electronic Engineering, Nanyang Technological University, 50 Nanyang Avenue, 639798 Singapore, Singapore
E-mail: munho.kim@ntu.edu.sg
[2)]Department of Materials Design and Innovation, University at Buffalo, The State University of New York, Buffalo, NY 14260, USA
[3)]Low Energy Electronic Systems (LEES), Singapore MIT Alliance for Research and Technology (SMART), 1 Create Way, Singapore 138602 Singapore

[*] Corresponding Author.

Email address: munho.kim@ntu.edu.sg (Munho Kim)

ABSTRACT

Interdigitated photodetectors (IPDs) based on the two-dimensional electron gas (2DEG) at the AlGaN/GaN interface have gained prominence as high sensitivity ultraviolet (UV) PDs due to their excellent optoelectronic performance. However, most 2DEG-IPDs have been built on rigid substrates so far, leading to the limited use for flexible and wearable applications. We demonstrate high performance flexible AlGaN/GaN 2DEG-IPDs using AlGaN/GaN 2DEG heterostructure membranes, whose great material quality is enabled by forming 8-inch AlGaN/GaN on insulator (AlGaN/GaNOI) substrates. The interdigitated AlGaN structure has been elaborately utilized to reduce dark current by disconnecting the conductive channel at the heterostructure interface. In addition, photocurrent can be boosted by the escaped carriers from the 2DEG. The flexible

AlGaN/GaN 2DEG-IPDs outperform most flexible UV photodetectors reported up to now. Therefore, the demonstration represents significant advances in the field of UV optoelectronic devices.

KEYWORDS. ultraviolet; flexible photodetectors; AlGaN/GaN; piezoelectric; XOI.

Introduction

Over the past decades, GaN has gained prominence as an ideal material platform for ultraviolet (UV) photodetectors (PDs) because of its large direct bandgap energy of 3.4 eV, superior durability in high-temperature and radiation-rich environments, and matured GaN high electron mobility transistor (HEMT) fabrication technology.[1-3] Many types of GaN-based PDs have been demonstrated, based on p-i-n, Schottky barrier, avalanche, and metal-semiconductor-metal (MSM) structures, but these GaN PDs suffer from low responsivity (<5 A/W), which falls behind the requirement of state-of-the-art optoelectronic applications.[4-8] To increase the responsivity, PD based on AlGaN/GaN HEMT structure was proposed.[9,10] Attributed to the extraordinary high carrier mobility at the interface of the AlGaN/GaN heterojunction, AlGaN/GaN HEMT based PDs have demonstrated extremely large responsivity (over 10^3 A/W). However, the highly conductive channel in AlGaN/GaN heterojunction also enlarged the dark current, thus causing the degradation of optoelectronic performance, such as high dark current, low photo-to-dark current ratio, and poor UV/visible (VIS) rejection ratio. Although the responsivity was increased, the high dark current has become the main bottleneck that significantly limits the application of AlGaN/GaN HEMT based PD. Therefore, development of the GaN PDs with both high responsivity and low dark current remained a major challenge. In 2011, Martens et al. reported a PD architecture

based on the two-dimensional electron gas (2DEG) at the interface of AlGaN/GaN heterojunction.[11] This scheme effectively reduced the dark current (*i.e.*, 50 nA at a bias of 100 V) by disconnecting the conductive channel at the heterostructure interface, and, most importantly, maintained the high responsivity (*i.e.*, 7×10^4 A/W at 312 nm) though a 2DEG induced internal gain mechanism simultaneously. Recently, Satterthwaite et al. optimized the 2DEG based PD based on the symmetrical interdigitated structure, and thus obtained a large responsivity of 7800 A/W, a high UV/VIS rejection ratio of 10^6, as well as a record high normalized photo-to-dark current ratio of 6×10^{14} W^{-1}.[12] Accordingly, such a device scheme based on 2DEG interdigitated PD (2DEG-IPD) has become the building blocks towards next-generation GaN UV PDs without the traditional limit in low responsivity or high dark current.

Flexible UV PD is one of the important technological elements for a wide range of future applications including smart health-monitoring, wearable human-machine communication, and versatile intelligent monitoring systems because it can stably detect UV-regime input signals without being affected by visible light.[13-16] However, while the performance of the rigid form of GaN-based UV PDs has been greatly improved with various structural innovations, a flexible version of GaN-based UV PDs remains in its' infancy and their performance is far behind compared with that of the rigid counterparts. Typically, flexible GaN-based UV PDs suffer from low responsivity and relatively high dark current due to a thinness of the active material and unoptimized device structures, in other words, the absence of a high-quality freestanding GaN material that has its' bulk single crystallinity as well as good mechanical durability.[17,18]

In recent years, various approaches have been reported to demonstrate free-standing crystalline GaN membranes that fulfill aforementioned requirements such as laser lift-off (LLO), conductivity-based selective etching, substrate removal *via* XeF_2 etching, and lift-off *via* a 2D buffer layer.[17] While single-crystalline GaN membranes can be obtained through these approaches, each respective method has its limitations.[19-22] For example, the LLO method requires a sophisticated laser setup for the lift-off and is only applicable to GaN layers grown on sapphire substrates. In addition, released GaN membranes suffer from unbalanced strain and rough interface.[23] The conductivity-based selective etching method restricts the types of releasable heterostructure GaN membranes because highly doped GaN layer is used as a sacrificial layer.[21] The drawback of the substrate removal *via* XeF_2 etching is that the position of GaN membrane-based devices cannot be controlled freely because the position of GaN device is decided in the wafer bonding-debonding process prior to the XeF_2 etching step.[19] Finally, the 2D layer-assisted lift-off method requires a complex growth process.[22] Therefore, a facile and reliable release of AlGaN/GaN heterostructure membranes is critically important for flexible GaN optoelectronics.

On the other hand, high-quality semiconductor membranes have been created using a semiconductor on insulator (XOI) wafer *via* a sacrificial chemical etching such as Si, Ge, III-V, GaN, and SiC membranes.[24-26] This method is well-suitable for low-cost and large-scale integration of membrane-based devices and circuits because the size of the SOI substrates has been extended to a full 12 inches. Therefore, GaN membranes that are produced from GaN-on-insulator (GaNOI) wafers are highly desirable for the development of cost-effective and high performance large-scale GaN-based flexible applications. Moreover, it is possible to create freestanding AlGaN/GaN 2DEG heterostructure membranes directly from the GaNOI wafer which allows us to adopt the advanced GaN-technology into

GaN flexible applications. However, the well-known method for producing XOI wafer, *i.e.*, a Smart Cut technology, cannot be used for the GaNOI wafer fabrication, because the hydrogen implantation and high-temperature process can ruin the delicate AlGaN/GaN heterostructures.

In this study, we present a viable approach to create free-standing AlGaN/GaN 2DEG heterostructure membranes directly from an 8-inch GaNOI substrate. We further demonstrate high-performance flexible AlGaN/GaN 2DEG-IPDs based on the released AlGaN/GaN 2DEG heterostructure membranes and achieve a strong photocurrent gain and an extremely low dark current under both flat and bent conditions. We also provide a detailed mechanism for high photogeneration of flexible 2DEG-IPDs as well as the effects of mechanical bending and high temperature on the device performance. Our research suggests that the realization of AlGaN/GaN 2DEG-IPD could be an effective approach to develop high-performance flexible UV PDs. Another broader impact of this research is the good process compatibility with other AlGaN/GaN based devices such as AlGaN/GaN HEMTs. In addition, this technique can be implemented in other AlGaN/GaN based heterojunction devices such as light-emitting diodes (LEDs) because their device structures can be also grown on Si substrates.[17] Therefore, a method of creation of high-quality AlGaN/GaN 2DEG heterostructure membrane directly from a GaNOI wafer provides a viable approach that is compatible with existing semiconductor foundry processes thus enables us to realize high-performance flexible GaN electronics and optoelectronics.

Result and discussion

Strategy of AlGaN/GaN 2DEG heterostructure membrane release from GaNOI. 8-inch AlGaN/GaNOI substrates were fabricated using the combination of epitaxial growth of AlGaN/GaN layers on Si, wafer bonding, and removal of the backside Si substrates. The schematic fabrication process

for the AlGaN/GaNOI substrate was shown in Figure 1(a). The fabrication process began by the epitaxial growth of thin heterojunction AlGaN/GaN 2DEG layers composed of capping GaN (3 nm)/AlGaN (30 nm)/AlN (1 nm)/GaN (600 nm) grown on a 1000 nm buffer layer on a Si (111) substrate. Then, AlGaN/GaN on Si substrate was bonded with a SiO_2 on Si substrate, followed by the removal of backside Si by KOH etching. The exposed AlGaN/GaN buffer layer was covered by SiO_2 and SiN and the substrate was subsequently bonded with SiN/SiO_2 on a Si carrier substrate. Epitaxially grown AlGaN/GaN structure was sandwiched by the top and bottom Si substrates. Removal of the top Si finalized the fabrication of AlGaN/GaNOI substrates. This wafer-scale integration method based on two stage wafer bonding enabled us to demonstrate the largest possible foundry manufacturable wafers, 8-inch AlGaN/GaNOI substrates.

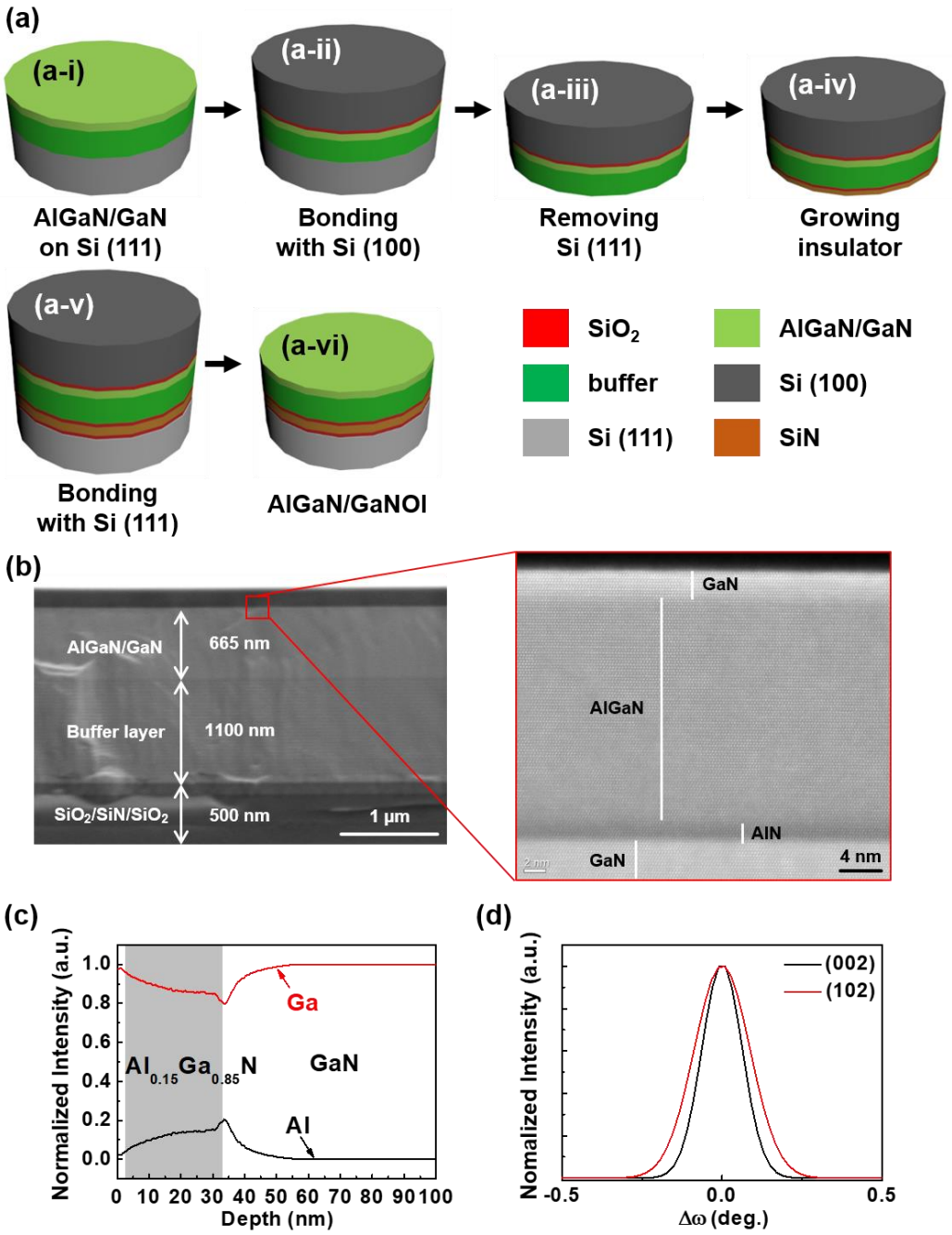

Figure 1. a) Schematic fabrication process of the AlGaN/GaNOI substrates: i) Grow AlGaN/GaN heterojunction on Si (111) substrate. ii) Bond AlGaN/GaN heterojunction to a Si handling substrate. iii) Remove backside Si (111) by KOH etching. iv) Deposit SiO_2 and SiN insulator layers on the backside. v) Bond insulator layers with Si (001) substrate. vi) Remove the handling substrate. b) Cross-sectional SEM and zoom-in HRTEM images of AlGaN/GaNOI material stack. c) SIMS depth

profile of AlGaN/GaN heterostructure. d) XRD rocking curve scans on (002) and (102) axis for estimating the densities of screw- and edge-type threading dislocations in AlGaN/GaNOI.

Figure 1(b-d) show the various microstructural properties of the manufactured AlGaN/GaNOIs. The cross-sectional SEM image clearly indicates that the abrupt interfaces were obtained among AlGaN/GaN, buffer, and sacrificial layers. Figure 1(b) shows the cross-sectional HRTEM image of AlGaN/GaN heterostructure membrane. It reveals that the high-quality atomically abrupt interface was achieved between the GaN, AlGaN, and AlN layers. Figure 1(c) shows the secondary ion mass spectrometry (SIMS) profile of Ga and Al traced from the top 100 nm of AlGaN/GaNOI. The red and black lines represent the concentrations of Ga and Al, respectively. SIMS analysis revealed that the nearly 30 nm thick AlGaN layer was formed on top of the undoped GaN with the Ga and Al concentrations of 85 and 15%, respectively. Moreover, the threading dislocation density of AlGaN/GaNOI was characterized by X-ray diffraction (XRD) rocking curve measured along (002) and (102) planes (Fig. 1(d)). The screw-type (D_{screw}) and edge-type (D_{edge}) threading dislocation densities can be determined by the following equations:[27]

$$D_{screw} = \frac{b_{(002)}^2}{4.35 b_{edge}^2} \quad (1)$$

$$D_{edge} = \frac{b_{(102)}^2 - b_{(002)}^2}{4.35 b_{edge}^2} \quad (2)$$

where the b_{screw} and b_{edge} are defined as the screw-type and edge-type Burgers vector length of GaN, and the $\beta_{(002)}$ and $\beta_{(102)}$ are the full width at half maximum (FWHM) of the (002) and (102) rocking curves, respectively. The $\beta_{(002)}$ and $\beta_{(102)}$ of AlGaN/GaNOI were extracted to be 623 and 936 arcs, respectively. Accordingly, the screw-type and edge-type threading dislocation intensities were calculated to be 7.65 ×

10^8 and 3.05×10^9 cm^{-2}, respectively. To further study the effect of the GaNOI processing, the rocking curve of as-grown AlGaN/GaN on Si substrate was measured (Fig. S1). The $\beta_{(002)}$ and $\beta_{(102)}$ of the as-grown AlGaN/GaN on Si were measured to be 540 and 756 arcs, leading to the D_{screw} and D_{edge} of 5.80×10^8 and 1.48×10^9 cm^{-2}, respectively. Although the crystalline quality of AlGaN/GaN heterostructure was slightly degraded, the D_{screw} and D_{edge} values of AlGaN/GaNOI are comparable to those of AlGaN/GaN heterostructures grown on conventional substrates (*i.e.*, on Si: $D_{screw} = 6.4 \times 10^9$ cm^{-2}, $D_{edge} = 1.1 \times 10^{10}$ cm^{-2} and on sapphire: $D_{screw} = \sim 2 \times 10^8$ cm^{-2}, $D_{edge} = \sim 2 \times 10^9$ cm^{-2}).[28,29]

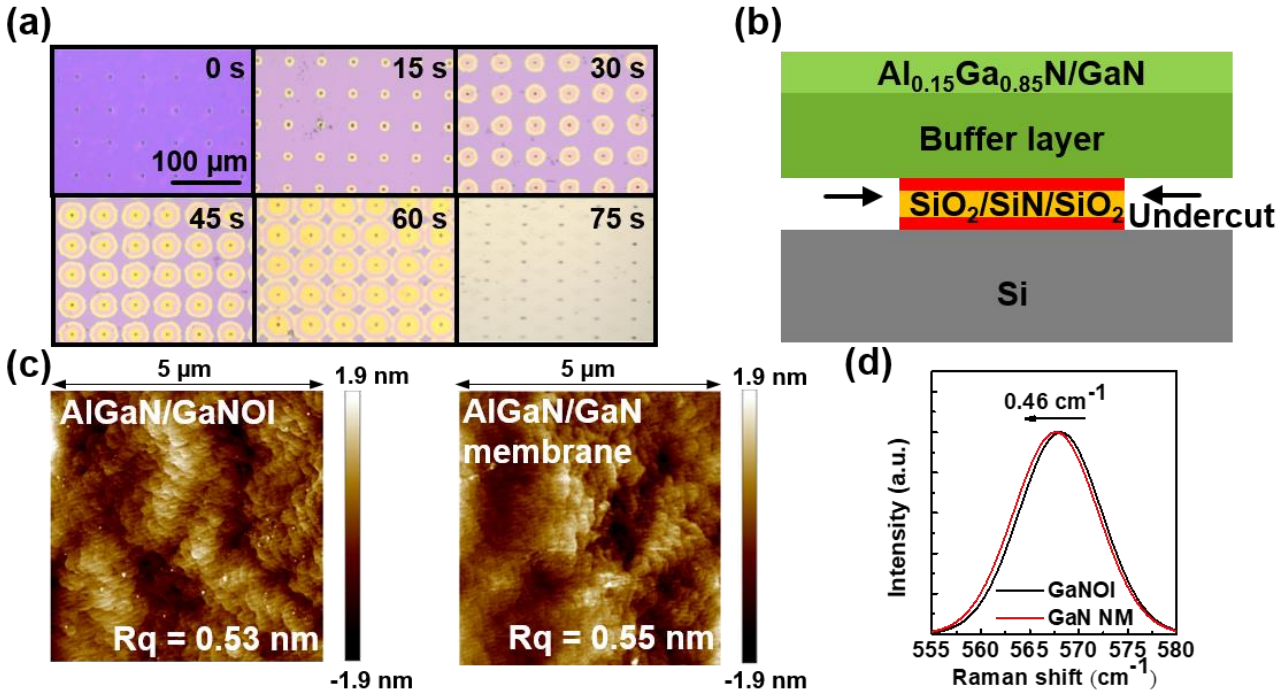

Figure 2. a) Top view images of the patterned AlGaN/GaNOI surface show the release of AlGaN/GaN 2DEG heterostructure membranes after the undercut etching times of 15, 30, 45, 60 and 75 seconds, respectively. b) Schematic cross-section of the AlGaN/GaNOI during the undercut. c) Top view AFM images of the AlGaN/GaN surfaces before and after undercut. d) Raman scan of E_2^H peak of AlGaN/GaNOI and the peak shift after AlGaN/GaN 2DEG heterostructure membrane is released.

The fabrication of free-standing releasable AlGaN/GaN 2DEG heterostructure membranes began with the photolithography (membrane size: 2 × 2 mm^2), followed by chlorine-based inductively coupled plasma reactive-ion etching (ICP-RIE) to pattern etching via arrays (size: 3 × 3 μm^2 and distance: 50 μm). These etching via arrays facilitate the access of etching solution, leading to the efficient undercut process. Subsequently, the samples went through the undercut process in hydrofluoric acid (HF, 49%) solution, where SiO_2/SiN/SiO_2 sacrificial layers were completely etched away. The evolution of the undercut progress was recorded by the optical microscope as shown in Figure 2(a). The bright circles observed in the images after the undercut times of 15 to 60 seconds are attributed to the formation of overhang regions, where the sacrificial layers are laterally etched by HF as illustrated in Figure 2(b). Besides, it was clearly observed that the bright circles expanded as the undercut time increases and they were eventually coalesced at 60 seconds, indicating the undercut process was nearly completed. After 75 seconds undercut, the AlGaN/GaN 2DEG heterostructure membranes were completely released and ready to be transferred to any arbitrary substrates. It has been reported that HF can etch essential metals (*e.g.*, Ti and Au) required to form ohmic contact on AlGaN/GaN surface.[30] Therefore, a short undercut time is beneficial because it can minimize damages to Ti/Al/Ti/Au-based ohmic contact of AlGaN/GaN devices.

Figure 2(c) shows the 2D AFM surface images of AlGaN/GaNOI and transfer-printed AlGaN/GaN 2DEG heterostructure membrane, respectively. A similar surface roughness (R_q = 0.55 nm) was measured for the AlGaN/GaN 2DEG heterostructure membrane compared to that of the AlGaN/GaNOI (R_q = 0.53 nm), indicating that smooth surface was maintained during the transfer process. The state of stress in the AlGaN/GaN structure before and after undercut was measured using

Raman spectroscopy by evaluating the shift in the GaN E_2^H mode. Figure 2(d) shows the E_2^H mode measured from the AlGaN/GaNOI and the released AlGaN/GaN 2DEG heterostructure membrane, respectively. The distinct E_2^H peak was located at 568.13 cm^{-1} for AlGaN/GaNOI, while the E_2^H peak was blue shifted to 567.67 cm^{-1} for the free-standing membrane. The stress can be evaluated by the following equation:[21]

$$\Delta\omega_{E2} = k_{Raman,a} \cdot \Delta\sigma \quad (3)$$

where $\Delta\omega_{E2}$ is the shift value of E_2^H peak, $\kappa_{Raman,a}$ is the Raman calibration constant (4.2 $cm^{-1}GPa^{-1}$), and σ is the n-plane biaxial stress.[31] The $\Delta\sigma$ was determined to be 110 MPa, which indicated that the compressive stress of 110 MPa in AlGaN/GaNOI was relaxed after the undercut. This stress relaxation might be attributed to the undercut process, which separated the insulator and AlGaN/GaN heterojunction, and thus releasing the stress caused by the lattice mismatch and the process-induced thermoelastic effects from the coefficient of thermal expansion mismatch.[32]

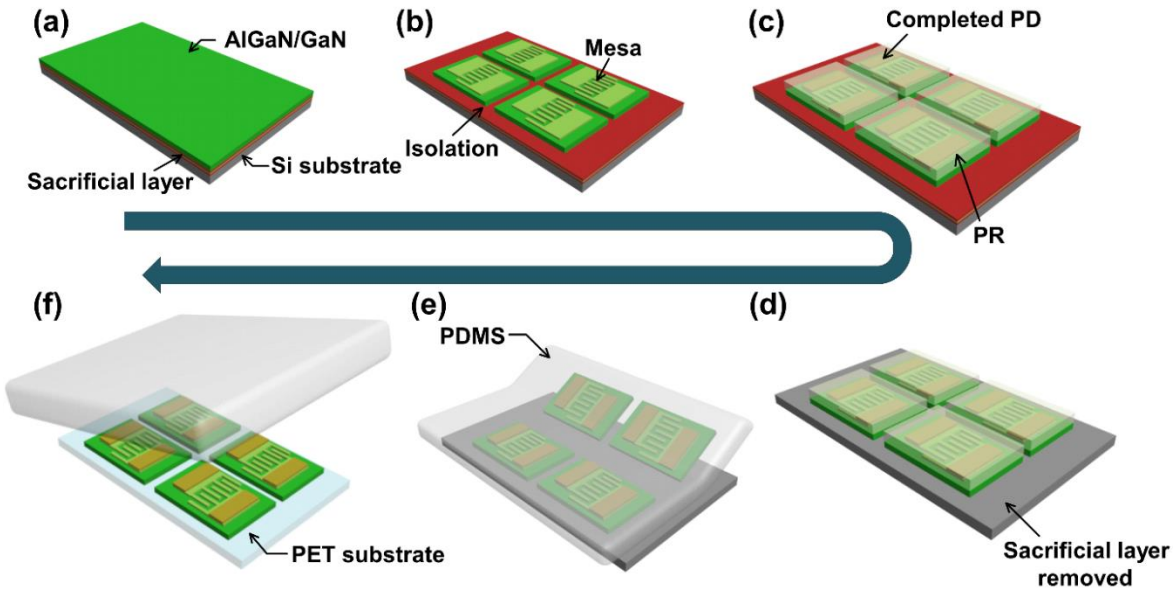

Figure 3. Schematic illustration of the fabrication process of AlGaN/GaN 2DEG-IPDs on a PET substrate: a) Fabrication of AlGaN/GaNOI substrate. b) Mesa structure and device active region are isolated by ICP-RIE. This step exposes the underlying sacrificial layer. c) Devices are fabricated on AlGaN/GaNOI and protected by PR. d) The sacrificial layer is etched by HF. e) Released devices are picked up by a PDMS stamp. f) Devices are transfer-printed on a PET substrate.

Flexible AlGaN/GaN 2DEG-IPDs. We fabricated flexible AlGaN/GaN 2DEG-IPDs to demonstrate the advantage of the AlGaN/GaN 2DEG heterostructure membranes towards high performance UV optoelectronics. Figure 3 outlines the procedure for manufacturing AlGaN/GaN 2DEG-IPDs on a PET substrate. The fabrication process began by isolating the AlGaN/GaNOI, followed by AlGaN mesa-etching to form an array of AlGaN/GaN 2DEG-IPD on GaN (Fig. 3(a) and (b)). Each device consisted of 5 pairs of interdigital AlGaN electrodes with the length, width, and spacing of 25, 5, and 5 μm, respectively. Post mesa-isolation was performed, followed by the deposition of a standard Ti/Al/Ti/Au (20/150/40/60 nm) ohmic metal stack on AlGaN. Ohmic contact was formed by the activation *via* rapid thermal annealing at 850 ˚C in N_2 ambient for 30 seconds. The XRD patterns of the as-prepared AlGaN/GaN membranes before and after annealing are shown in Figure S2. It is found that the $\beta_{(002)}$ of AlGaN/GaN membrane before and after annealing were extracted to be 623 and 645 arcs. In addition, the $\beta_{(102)}$ values were measured to be 936 and 937 arcs, respectively. Therefore, it reveals that the effect of annealing on the crystalline quality of the AlGaN/GaN membranes is negligible. Photoresist (PR) was patterned on AlGaN/GaN 2DEG-IPD as a protection layer to avoid any potential degradation of the ohmic contact by HF etching (Fig. 3(c) and 3(d)). After the completion of undercutting, the free-standing devices were picked up by an elastomeric PDMS stamp and transfer-printed on a PET substrate coated with an adhesive SU-8 2002 layer (Fig. 3(e) and 3(f)).

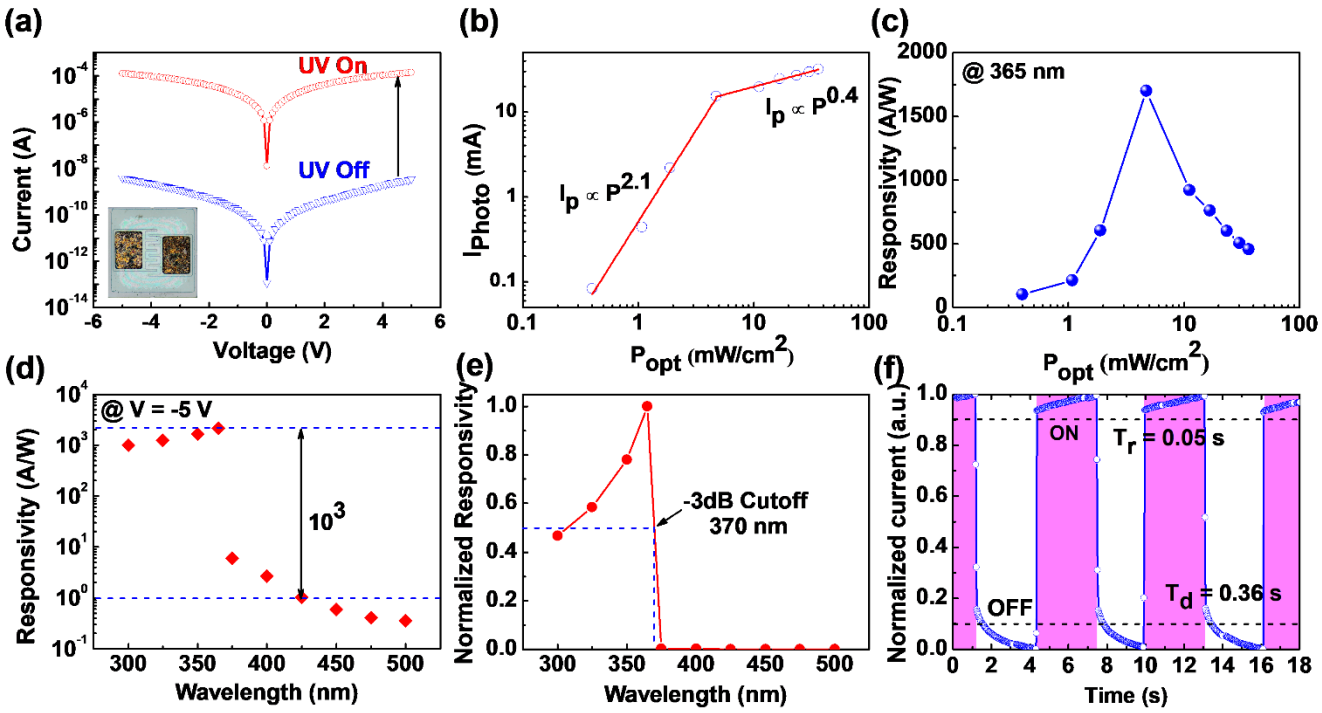

Figure 4. Device performance of flexible AlGaN/GaN 2DEG-IPD under flat condition: a) I_{dark} and I_{photo} at a wavelength of 365 nm. Inset shows the top view microscopic image of the fabricated device on PET. b and c) I_{photo} and responsivity dependence of various optical powers at 365 nm. d) Spectral response at -5 V. e) Normalized spectral response of the device. f) Normalized transient response of the device.

Optoelectronic characterizations of flexible AlGaN/GaN 2DEG-IPDs. Figure 4 shows a sequence of optoelectronic characteristics of flexible AlGaN/GaN 2DEG-IPDs under flat condition. The inset in Figure 4(a) shows an optical microscopy image of the fabricated AlGaN/GaN 2DEG-IPD. As shown in Figure 4(a), a low dark current (I_{dark}) of 3.85 nA and a high photocurrent (I_{photo}) of 0.13 mA were achieved at a bias voltage of -5 V, leading to a high ratio of dark and photocurrent of 3.4×10^4. The low I_{dark} was attributed to the interdigital etching of the $Al_{0.15}Ga_{0.85}N$ layer, which inhibits the 2DEG introduced high I_{dark} exhibited in typical AlGaN/GaN PDs. In addition, the high I_{photo} was due to the existence of the

2DEG layer, and thus demonstrating the effectiveness of the AlGaN/GaN 2DEG-IPD. Responsivity is one of the most important figure-of-merits for PDs, which is defined as[33]

$$R = \frac{I_{photo} - I_{dark}}{P_{opt} A} \tag{4}$$

where P_{opt} is the incident light power intensity, and A is the effective illuminated area of the device. Responsivity was calculated to be 1670 A/W at -5 V, which significantly exceeds the 100% quantum efficiency, indicating the existence of an external gain mechanism in the device.

To further investigate the gain mechanism, the power intensity dependent photoresponse measurements were performed by varying the power intensity from 0.4 to 36.3 mW/cm^2 at a fixed bias of -5 V (Figure 4b). The measured I_{photo} was fitted by the power law described in the equation below:[34]

$$I_{photo} = CP_{opt}^{\ q} \tag{5}$$

where C is a constant for a fixed wavelength, and θ is the empirical coefficient. For conventional PDs, θ < 1 indicates the trap influenced carrier transport in the channel, while θ > 1 suggests the photocurrent gain mechanism.[35,36] However, for our 2DEG-IPD, θ < 1 should be also attributed to the reduced gain at high power intensity region, as shown in Figure S3. As shown in Figure 4(b), a θ value of 2.1 was extracted by a linear fitting of the measured I_{photo} data when the power intensity is smaller than 4.7 mW/cm^2, while 0.4 was extracted when the power intensity was larger than 4.7 mW/cm^2. The decreased gain at high power intensity region is ascribed to the saturation in increase of escaped electrons. Therefore, the gain mechanism is dominant in both low and high-power intensity regions. One possible mechanism of such high gains should be the escaped electrons from 2DEG to the GaN conduction band under the UV-on state. Detailed analysis on the gain mechanism will be discussed at a later part of this

paper. Normalized photo-to-dark current ratio (NPDR) is another important performance metric for PD, which expressed as:[37]

$$NPDR = \frac{I_{photo}/I_{dark}}{P_{opt}A} = \frac{R}{I_{dark}} \quad (6)$$

Here, the NPDR was calculated to be 4.3×10^{11} W^{-1} at -5 V, which is at least 2 orders of magnitude higher than those of flexible GaN PDs (Table 1). Such high responsivity and NPDR suggest that our AlGaN/GaN 2DEG heterostructure membranes are the excellent material platform toward its application for high performance flexible GaN optoelectronic and photonic devices.

Figure 4(d) presents the spectral response of the AlGaN/GaN 2DEG-IPD at a wavelength range from 300 to 500 nm. The external bias and incident power intensity were fixed at -5 V and 4.7 mW/cm^2, respectively, during measurement. The maximum responsivity of 1670 A/W was measured at 365 nm. The UV/VIS rejection ratio (RR) between 365 and 425 nm of the AlGaN/GaN 2DEG-IPD was 2×10^3, which is comparable to those of the previously reported GaN PDs.[9,38,39] Such an excellent wavelength selectivity guarantees a true, effective, and ultrasensitive photodetection of UV light. Moreover, the -3 dB cutoff wavelength of the AlGaN/GaN 2DEG-IPD was extracted to be 370 nm (Fig. 4(e)), further confirming the UV photodetection property of our AlGaN/GaN 2DEG-IPD.

Figure 4(f) shows the transient response of the AlGaN/GaN 2DEG-IPD at -5 V. UV light with a wavelength of 350 nm and an incident power intensity of 4.7 mW/cm^2 was repeatedly switched on and off with time intervals of 3 seconds. It was shown that our device could be reversibly modulated by the UV illumination, which demonstrates an excellent reproducibility and stability during operation. The rise time (T_r, defined as the time required for the current increase from 10 to 90% of the peak value) and decay time (T_d) were extracted to be 50 and 360 ms, respectively. The relatively large T_d was attributed

to the persistent photoconductivity (PPC) effect, where the photoexcited electrons transferred from deep-level impurities to the $Al_{0.15}Ga_{0.85}N$ layer cause a slow recovering process. In addition, it was observed that the I_{photo} did not completely recover to the initial I_{dark} value within a 3000 ms window, as shown in Figure S4, which further indicates the presence of PPC. Similar trends have been frequently reported by AlGaN/GaN PDs.[40] Table 1 provides the performance comparison among previously reported flexible UV PDs. It can be concluded that our flexible device has superior UV detection properties, especially the NPDR, which is at least one order of magnitude higher than others.

Table 1. Comparison of photodetection performance among the AlGaN/GaN 2DEG-IPD and previously reported flexible UV PDs.

detector type	bias (V)	λ (nm)	RR	I_{dark} (A)	R (A/W)	NPDR (W^{-1})	T_r (s)	T_d (s)	reference
AlGaN/GaN 2DEG-IPD	-5	365	2×10^3	3.85×10^{-9}	1670	4.3×10^{11}	0.05	0.36	This work
GaN self-powered PD	0	NA	NA	3.53×10^{-11}	0.03	8.6×10^8	NA	NA	Peng et al.[41]
GaN nanowire PD	5	360	$\sim10^3$	5.60×10^{-8}	70.4	1.3×10^9	NA	NA	Weng et al.[42]
ZnO PD	15	360	NA	1.04×10^{-8}	2.2	2.1×10^8	0.2	0.3	Zhang et al.[43]
ZnO nanowire PD	5	365~370	NA	NA	4.3	2.0×10^9	12	230	Núñez et al.[44]
amorphous Ga_2O_3 PD	5	270	< 10	$\sim1.5 \times 10^{-6}$	9.7	6.5×10^6	1	1.1	Tak et al.[45]
amorphous InGaZnO PD	20	400	10	7.06×10^{-6}	36000	5.1×10^9	NA	NA	Zhang et al.[34]
MoS_2/g-C_3N_4 hybrid PD	-9	365	NA	1×10^{-9}	0.5	5×10^{10}	0.06	0.10	Velusamy et al.[46]
$CsPbBr_3$ perovskites PD	1	450	NA	4.8×10^{-8}	0.0029	6×10^4	0.26	0.28	Zhang et al.[47]
SnS nanoflake PD	5	380	NA	5×10^{-10}	3×10^{-6}	6×10^3	0.67	0.52	Mahdi et al.[48]

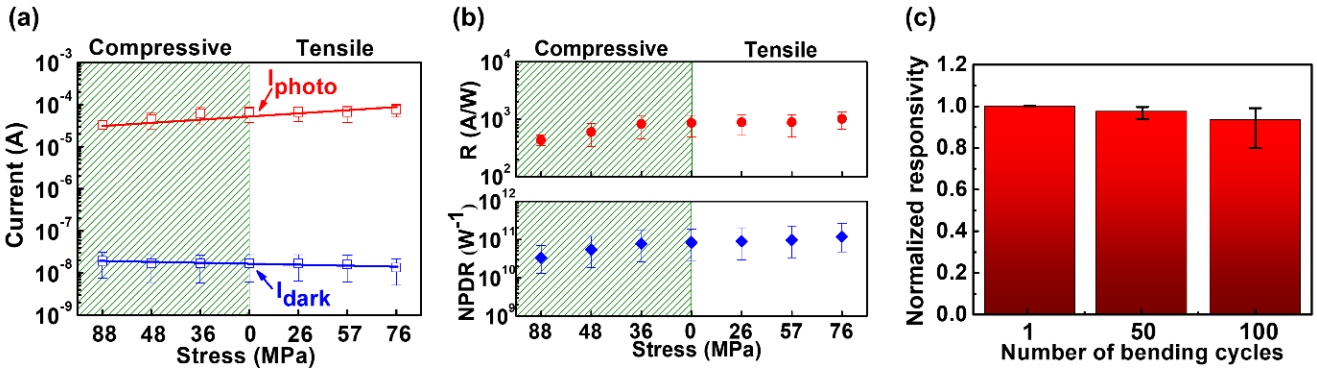

Figure 5. Device performance of flexible AlGaN/GaN 2DEG-IPD under applied external stress: a) Variation of I_{dark} and I_{photo} as a function of the stress. b) Extracted responsivity and NPDR of the devices at different external stresses, c) Normalized responsivity of the devices after multiple bending cycles measured under the concave fixture with a bending radius of 20 mm at 365 nm.

Analysis of the influence of the external stress on the device performance. In order to evaluate the effect of the external strain on the device performance, the flexible AlGaN/GaN 2DEG-IPDs were measured under bent conditions, where the devices were conformally placed on the bending fixtures with concave and convex curvatures. The applied strains in the device were extracted by evaluating the GaN E_2^H in the Raman spectra, as shown in Figure S5. Figure 5 presents the optoelectronic characteristics of our AlGaN/GaN 2DEG-IPDs under different strain values. To minimize the measurement error, the photoresponse curves of three individual AlGaN/GaN 2DEG-IPDs have been measured under various strains (Fig. S6). The average value of I_{dark} increased from 17 to 19.5 nA, while the average I_{photo} decreased from 64.8 to 32.5 µA under uniaxial compressive strain. On the other hand, when the uniaxial tensile strain was applied, the average I_{dark} decreased from 17 to 13.5 nA, whereas the average I_{photo} increased from 64.8 to 76.4 µA. The opposite trend observed from I_{dark} and I_{photo} variations is attributed to piezo-phototronic and piezo-resistive effects under the tensile and compressive strains, respectively. Moreover, responsivity and NPDR values of AlGaN/GaN 2DEG-IPDs were calculated under tensile and

compressive strains (Fig. 5(b)). Both responsivity and NPDR were gradually increased under tensile strain and decreased under compressive strain. Specifically, responsivity was increased 16% under 76 MPa tensile stress and decreased by 54% under 88 MPa compressive stress. Similarly, NPDR was increased by 38% under tensile stress and decreased by 63 % under compressive stress. The results indicate that the UV detective performance of our AlGaN/GaN 2DEG-IPD can be effectively controlled by the external strains. The optoelectronic performance of 2DEG-IPD under different external strain is summarized in Table 2. In addition, the normalized responsivity after multiple bending cycles is presented in Figure 5(c). The error bars on the plot represent standard deviations over measurements taken on three devices. Responsivity remained almost unchanged after repetitive bending up to 100 cycles, demonstrating the excellent resistance against continuous bending stress.

Table 2. Photoelectronic performance of the flexible AlGaN/GaN 2DEG-IPD under different external strain.

Stress (MPa)		bias (V)	λ (nm)	I_{dark} (A)	I_{photo} (A)	R (A/W)	NPDR (W^{-1})
	88			7.64×10^{-9}	3.98×10^{-5}	529	6.92×10^{10}
Compressive	48			6.96×10^{-9}	6.40×10^{-5}	849	1.22×10^{11}
	36			6.50×10^{-9}	8.52×10^{-5}	1130	1.74×10^{11}
Flat	0	-5	365	6.12×10^{-8}	8.70×10^{-5}	1160	1.89×10^{11}
	26			5.76×10^{-9}	8.94×10^{-5}	1190	2.06×10^{11}
Tensile	57			5.38×10^{-9}	9.08×10^{-5}	1210	2.24×10^{11}
	76			5.14×10^{-9}	1.01×10^{-4}	1340	2.60×10^{11}

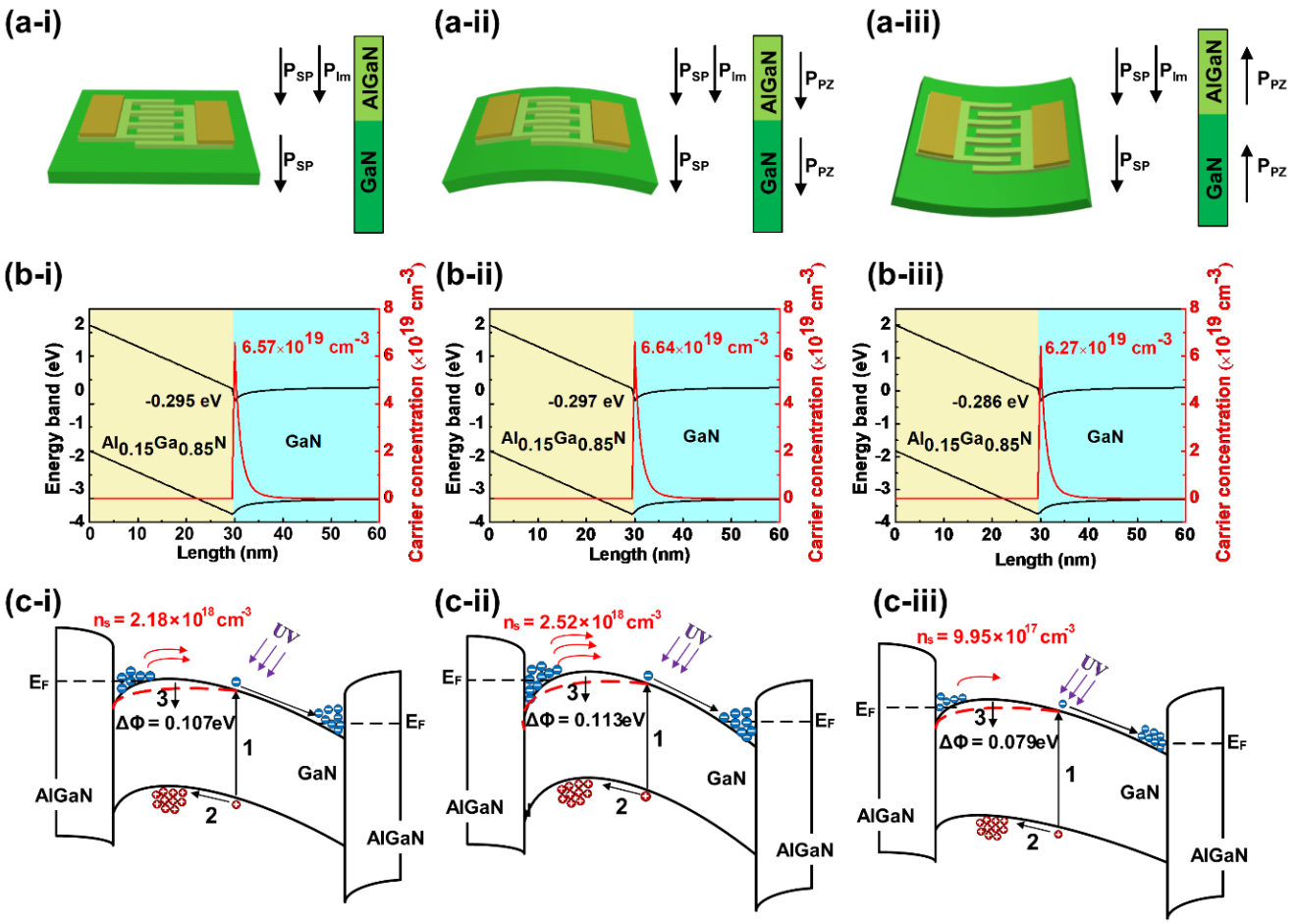

Figure 6. a) Schematic illustration of polarizations in AlGaN/GaN heterostructures under i) flat, ii) tensile, and iii) compressive strain conditions. b) Calculated energy band diagram and the corresponding carrier distribution at the interface of AlGaN/GaN heterostructures under i) flat, ii) tensile, and iii) compressive strain conditions. c) The schematic band structures at AlGaN/GaN interface under UV-on state under i) flat, ii) tensile, and iii) compressive strain conditions.

We seek to explain the mechanism of the strain-modulation effect in AlGaN/GaN 2DEG-IPDs. Figure 5 presents the mechanism of the AlGaN/GaN heterostructure under flat, tensile, and compressive strain conditions, respectively. Owing to the non-centrosymmetric crystal structures of AlN and GaN, two different types of intrinsic polarizations are generated in the AlGaN/GaN heterojunction, which are the spontaneous polarization (P_{SP}) in both GaN and AlGaN and the lattice-mismatch induced

piezoelectric polarizations (P_{lm}) in AlGaN (Fig. 6(a)). The orientation of the P_{SP} and P_{lm} goes from the N atom to the nearest neighbor metal atom along the c-axis, thus forcing the electrons move towards a triangle-shaped potential well at the interface of AlGaN/GaN heterojunction, namely, 2DEG. The distributed band energy and electron concentration along the c-axis were calculated by self-consistent coupling solutions of 1D Schrodinger-Poisson equations (Fig. 6(b-i)). Here, we define the energy separation between the Fermi level and the bottom of the GaN conduction band as Φ_b. In addition, parameters of AlGaN and GaN layers are required for calculation, such as energy gap, relative dielectric constant, and polarization. Data are extracted from the previous report.[49] Accordingly, the Φ_b and the sheet carrier concentration (n_s) were calculated to be 0.295 eV and 6.57×10^{19} cm^{-3} for the AlGaN/GaN heterojunction without external strain. Once the heterojunction is bent, the stress will induce additional piezoelectric polarizations (P_{PZ}) in GaN and AlGaN along the c-axis, where polarity depends on the type of the strain. When tensile strain is applied, P_{PZ} exhibits the same direction with P_{SP} and P_{lm} (Fig. 6(a-ii)). The polarization of AlGaN and GaN layers can be calculated by the following quadratic expressions:[50]

$$P_{AlGaN} = P_{SP} + P_{lm} + e_{33}e_{\wedge} + 2e_{31}e_{//} + e_{311}e_{//}^2 + e_{333}e_{\wedge}^2 + e_{313}e_{//}e_{\wedge} \quad (7)$$

$$P_{GaN} = P_{SP} + e_{33}e_{\wedge} + 2e_{31}e_{//} + e_{311}e_{//}^2 + e_{333}e_{\wedge}^2 + e_{313}e_{//}e_{\wedge} \quad (8)$$

where e_{ij} and e_{ijk} are the nonlinear piezoelectricity coefficients, $e_{\wedge}$ is the external strain in the orthogonal direction, and $e_{//}$ is the external strain in the c-plane direction. Figure 6(b-ii) presents the calculated band diagram and carrier distribution of AlGaN/GaN heterojunction under 76 MPa tensile stress, where Φ_b and n_s are increased to 0.297 eV and 6.64×10^{19} cm^{-3}, respectively. These values indicate that tensile strain drives the electrons to the 2DEG, and thus increasing the barrier height, as well as the density of

trapped electrons. Hence, the current flow is suppressed by the increased Φ_b under the UV-off state, which is consistent with the decreased I_{dark} under tensile strain. When the compressive strain is applied, the P_{pz} in AlGaN/GaN heterojunction is reversed (Fig. 6(a-iii)), resulting in a decreased Φ_b of 0.286 eV and a reduced n_s of 6.27×10^{19} cm^{-3} (Fig. 6(b-iii)). Similarly, the decreased Φ_b leads to the increased I_{dark} under compressive strain.

Figure 6(c) presents the schematic band diagrams of flat and strained AlGaN/GaN 2DEG-IPD perpendicular to the c-axis under the UV-on state. As shown in Figure 6(c-i), the photoresponse mechanism of AlGaN/GaN 2DEG-IPD is governed by two dominant processes. Firstly, electron-hole pairs are generated by the illumination excitation with photon energies above the bandgap of GaN (process 1). Subsequently, the photo-generated holes drift towards the interface of AlGaN/GaN heterojunction and accumulate there, thus leading to an electrostatic lowering of the barrier height for electrons in the 2DEG, thereby allowing the electrons to escape from the quantum well and move into the conduction band (process 2, dashed red line). The illumination-induced carrier concentration change (Δn_s) in the AlGaN/GaN channel can be estimated by the following equation:[9]

$$\Delta n_s = \frac{\Delta I}{q v_n W} \tag{9}$$

where ΔI is the photo-generated current, v_n is the average electron velocity in the channel, and W is the device width. Besides, the thickness of 2DEG layer was assumed to be 1 nm. The Δn_s was calculated to be 2.18×10^{18} cm^{-3} for AlGaN/GaN 2DEG-IPD without external strain. Moreover, the Δn_s increased to 2.52×10^{18} cm^{-3} and decreased to 9.95×10^{17} cm^{-3} when the device was under the tensile and compressive strain, respectively (Fig. 6(c-ii) and (c-iii)). These values indicate that external strains can effectively tune the amount of the electrons, which were escaped from the 2DEG. Furthermore, the barrier height

lowering (ΔΦ) induced by the accumulation of photo-generated holes is another important parameter and can be extracted from the equation below:[12]

$$\Delta n_s = \frac{k_b T m^*}{\pi \hbar^2} \exp\left(-\frac{q(\Phi_b - \Delta\Phi)}{k_b T}\right) \quad (10)$$

where k_b is the Boltzmann constant, ħ is the Planck constant, and m^* is the effective mass of carriers in the channel. The determined value of ΔΦ was 0.107, 0.113, and 0.079 eV for AlGaN/GaN 2DEG-IPD under flat, tensile, and compressive external strain, respectively. Obviously, ΔΦ was increased under tensile strain and decreased under compressive strain, which exhibited the same trend with Φ_b. The mechanism of ΔΦ variation is also related to the introduced P_{PZ} by external strains. The tensile strain in GaN will push photo-generated holes towards the interface of AlGaN/GaN heterojunction along the c-axis, as depicted in Figure 6(a-ii), thereby increasing the density of accumulated holes as well as the ΔΦ at the interface. The compressive strain has a reverse effect on the photo-generated holes (Fig. 6(a-iii)), resulting in a decreased ΔΦ. It is noted from equation 11 that larger value of Φ_b corresponds to a smaller value of Δn_s, whereas the larger ΔΦ result in a larger Δn_s. Accordingly, the Δn_s variation under external strains was determined by the trading off effect between the Φ_b and ΔΦ variation. Under the tensile stress of 76 MPa, Φ_b and ΔΦ was increased with an amount of 0.002 eV and 0.006 eV, respectively. On the other hand, the Φ_b and ΔΦ was decreased with an amount of 0.01 and 0.028 eV when the compressive stress of 88 MPa was applied, respectively. Hence, ΔΦ variation plays a more critical role than Φ_b in determining the change of Δn_s under both tensile and compressive strains. According to the mechanism of AlGaN/GaN 2DEG-IPD, the gain (G) of our device is proportional to the Δn_s, as expressed by the equation 12:[12]

$$G = \frac{\mathrm{D} n_s m_e V}{F_{ph} W^2} \tag{11}$$

where μ_e is the electron mobility and F_{ph} is the photon flux per unit area. The G values of 4.53×10^5, 5.24×10^5, and 2.07×10^5 were obtained for AlGaN/GaN 2DEG-IPD under flat, 76 MPa tensile, and 88 MPa compressive stress, respectively. Therefore, 15.7% increase and 54.3% decrease of G were observed under 76 MPa tensile and 88 MPa compressive stress, respectively. This result further confirms that the external strain plays a significant role in manipulating the performance of our flexible AlGaN/GaN 2DEG-IPDs.

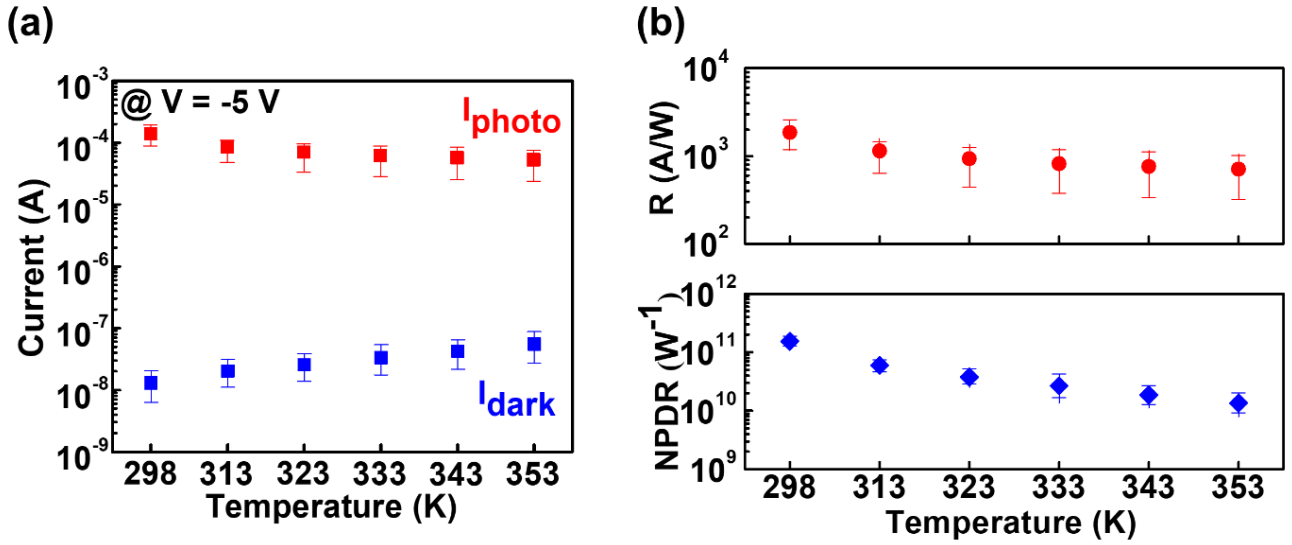

Figure 7. Device performance of flexible AlGaN/GaN 2DEG-IPD at high temperatures: a) I_{dark} and I_{photo} at -5 bias with increasing temperature up to 353 K. b) Responsivity and NPDR of the devices at elevated temperatures.

Device performance at high temperatures. The UV detection performance of flexible AlGaN/GaN 2DEG-IPD at high temperatures has been explored. Figure 7(a) presents I_{dark} and I_{photo} of three individual AlGaN/GaN 2DEG-IPDs at a bias of -5 V in a temperature range from 298 to 353 K. The error bars represent standard deviations of three samples (Fig. S7). The I_{photo} was measured at 365 nm under the

illumination intensity of 4.7 mW/cm^2. It was observed that I_{dark} was monotonically increased, while I_{photo} was gradually decreased upon increasing the temperature. Under dark condition, carriers in 2DEG-IPD transport across the Φ_b between AlGaN and GaN *via* thermionic emission, which requires a thermal energy to overcome the barrier height. Therefore, the increased temperature facilitates the Φ_b lowering and the tunneling of thermally activated electrons, leading to an increased current in GaN channel. When the devices are illuminated, electrons are escaped from the 2DEG due to photo-generated Φ_b lowering. Such a Φ_b lowering is much larger than the one caused by the increased temperature. On the other hands, when the temperature is increased, the scattering caused by the piezoelectric effects and acoustic deformation in AlGaN/GaN heterojunction becomes dominant, resulting in the decreased mobility. Therefore, the decreased photocurrent at higher temperatures can be explained by the mobility degradation. The responsivity and NPDR performance of AlGaN/GaN 2DEG-IPDs as a function of temperature were shown in Figure 7(b), where both responsivity and NPDR were reduced at high temperatures. Although the performance was slightly degraded at high temperatures, the responsivity (~10^3 A/W at 353 K) and NPDR (~10^{10} W-1 at 353 K) of our flexible 2DEG-IPDs remain high.

Conclusion

In summary, we have demonstrated flexible AlGaN/GaN 2DEG-IPD-based UV PDs using free-standing AlGaN/GaN 2DEG heterostructure membranes fabricated from AlGaN/GaNOI substrates *via* an unconventional release strategy. The microstructural, morphological, and crystalline properties of the transfer-printed AlGaN/GaN 2DEG heterostructure membranes were validated to be essentially identical to those from the bulk AlGaN/GaNOI. The flexible AlGaN/GaN 2DEG-IPDs could exhibit high

responsivity and NPDR that exceeded 1670 A/W and 4.3×10^{11} W^{-1}, respectively, mainly due to the excellent material quality of the single-crystalline AlGaN/GaN 2DEG heterostructure membranes. A significant piezo-phototronic behaviour was observed under strain, resulting from the piezoelectric-induced polarization at the heterostructure interface. Furthermore, our device maintained good optoelectronic characteristics in harsh environments such as multiple bending and high temperature. This result suggests that it is feasible to realize large-scale light-weight and flexible optoelectronics/electronics with outstanding performance toward various applications in wearable systems for personal UV monitoring, smart gloves/suits with UV detectivity, and electronic eye-type UV imagers. Therefore, the high performance flexible AlGaN/GaN 2DEG-IPDs with good durability could bring forth significant advances in the field of next-generation UV optoelectronic devices and circuits.

Methods

Fabrication and characterization of 8-inch AlGaN/GaNOI substrates. AlGaN/GaN heterostructure was grown on Si substrate by a low-pressure MOCVD. Triethylaluminum, triethylgallium, and ammonia were used as Al, Ga, and N precursors, respectively. 1.1 μm thick AlGaN quantum well was firstly deposited on top of Si substrate as a buffer layer, followed by a 600-nm undoped GaN. Subsequently, an undoped AlGaN barrier layer of 30 nm thickness with an Al-content of 15% was deposited. 8-inch AlGaN/GaN on Si(111) substrates were subsequently bonded with Si(100) handling substrates coated with a 200 nm SiO_2, followed by the removal of Si(111) substrates *via* a combination of mechanical grinding and KOH etching. Then, Si(100)/AlGaN/GaN substrates were bonded with Si(111) substrates

with 500 nm SiO_2/SiN/SiO_2 layers. Si(100) handling substrates were removed by the backside Si etching, leading to the complete fabrication of AlGaN/GaNOI substrates.

The cross-sectional layer structure, surface morphology, and crystal quality of the AlGaN/GaN heterojunction were characterized by Apreo-S Field Emission SEM, JEOL 2100F TEM, Bruker Dimension Edge AFM, and X'Pert3 MRD (XL) XRD, respectively. Profile of Ga and Al in AlGaN/GaN layers was traced by SIMS. A slow sputtering rate was used to analyze the surface region. Moreover, the strain values applied in AlGaN/GaN heterostructure were investigated by UHT S300 & WITEC Raman spectroscopy with a 532 nm laser focusing on a 1 μm diameter spot by using a 100× objective lens.

Fabrication of AlGaN/GaN 2DEG-IPDs on PET substrates. Device patterning and mesa-isolation of AlGaN/GaN were carried out by the Oxford Plasma Pro 100 ICP-RIE. Ohmic metal (Ti/Al/Ti/Au = 20/150/40/60 nm) was evaporated by Edwards Auto306 E-Beam and subsequently annealed at 850 ˚C for 30 seconds by the AS-One rapid thermal processing system. AZ 5214E PR was covered on each fabricated AlGaN/GaN 2DEG-IPD as a protective layer. AlGaN/GaNOI sample was undercuted for 90 seconds by a few drops of 49% HF solution, followed by DI water cleaning. Subsequently, a PDMS stamp was used to pick up the free-standing AlGaN/GaN 2DEG-IPDs and they were subsequently transferred on a PET substrate coated with 2 μm SU-8 2000 adhesive layer.

Optoelectronic measurements and analysis. The optoelectrical properties of AlGaN/GaN 2DEG-IPD were measured using a Keithley 4200 SCS Semiconductor Analyzer in the darkbox. UV light was illuminated directly from Horiba 150 W Xe Tunable Light Source using a Formfactor light wave probe. The Signatone High Temperature Hot Chuck System was used to carry out the I-V-Temp measurements of AlGaN/GaN 2DEG-IPD from room temperature to 80 ˚C with a 10 ˚C interval under ambient

condition. The optoelectrical properties of under different strain conditions were measured using various convex (tensile strain) and concave molds (compressive strain) that have different curve radii ranging from 110 to 20 mm.

ASSOCIATED CONTENT

Supporting Information

XRD rocking curve scans of AlGaN/GaN on Si and AlGaN/GaNOI, Gain of AlGaN/GaN 2DEG-IPD at various power intensities, Transient response of the 2DEG-IDT after the UV illumination turned off, Raman spectra under bent conditions, Current-voltage curves of three individual 2DEG-IDTs under the UV-on and UV-off states with convex and concave fixtures with various radius, and Device performance of three individual 2DEG-IDTs at high temperatures.

ACKNOWLEDGMENT

The work was supported by A*STAR Advanced Manufacturing and Engineering (AME) Young Individual Research Grant (YIRG) under Project A2084c0066 and partly by the National Research Foundation, Singapore, under its Competitive Research Program (CRP Award NRF-CRP19-2017-01). Prof. Seo acknowledges the National Science Foundation, USA (Grant number: ECCS - 1809077).

REFERENCES

(1) Tsai, Y.-L.; Lai, K.-Y.; Lee, M.-J.; Liao, Y.-K.; Ooi, B. S.; Kuo, H.-C.; He, J.-H. Photon Management of GaN-based Optoelectronic Devices via Nanoscaled Phenomena. *Prog. Quantum Electron.* **2016,** *49*, 1-25.

(2) Miller, R. A.; So, H.; Chiamori, H. C.; Suria, A. J.; Chapin, C. A.; Senesky, D. G. A Microfabricated Sun Sensor using GaN-on-sapphire Ultraviolet Photodetector Arrays. *Rev. Sci. Instrum.* **2016,** *87* (9), 095003.

(3) Strite, S.; Morkoç, H. GaN, AlN, and InN: A Review. *J. Vac. Sci. Technol. B* **1992,** *10* (4), 1237-1266.

(4) Parish, G.; Keller, S.; Kozodoy, P.; Ibbetson, J.; Marchand, H.; Fini, P.; Fleischer, S.; DenBaars, S.; Mishra, U.; Tarsa, E. High-Performance (Al,Ga)N-based Solar-Blind Ultraviolet p–i–n Detectors on Laterally Epitaxially Overgrown GaN. *Appl. Phys. Lett.* **1999,** *75* (2), 247-249.

(5) Katz, O.; Garber, V.; Meyler, B.; Bahir, G.; Salzman, J. Gain Mechanism in GaN Schottky Ultraviolet Detectors. *Appl. Phys. Lett.* **2001,** *79* (10), 1417-1419.

(6) Huang, Y.; Chen, D.; Lu, H.; Dong, K.; Zhang, R.; Zheng, Y.; Li, L.; Li, Z. Back-illuminated Separate Absorption and Multiplication AlGaN Solar-Blind Avalanche Photodiodes. *Appl. Phys. Lett.* **2012,** *101* (25), 253516.

(7) Wang, C.-K.; Chiou, Y.-Z.; Chang, S.-J.; Lai, W.-C.; Chang, S.-P.; Yen, C.-H.; Hung, C.-C. GaN MSM UV Photodetector with Sputtered AlN Nucleation Layer. *IEEE Sens. J.* **2015,** *15* (9), 4743-4748.

(8) Chang, S.; Chang, M.; Yang, Y. Enhanced Responsivity of GaN Metal–Semiconductor–Metal (MSM) Photodetectors on GaN Substrate. *IEEE Photon. J.* **2017,** *9* (2), 1-7.

(9) Khan, M. A.; Shur, M.; Chen, Q.; Kuznia, J.; Sun, C. Gated Photodetector based on GaN/AlGaN Heterostructure Field Effect Transistor. *Electron. Lett.* **1995,** *31* (5), 398-400.

(10) Kuan, T.-M.; Chang, S.-J.; Su, Y.-K.; Ko, C.-H.; Webb, J. B.; Bardwell, J. A.; Liu, Y.; Tang, H.; Lin, W.-J.; Cherng, Y.-T. High Optical-Gain AlGaN/GaN 2 Dimensional Electron Gas Photodetectors. *Jpn. J. Appl. Phys.* **2003,** *42* (9R), 5563.

(11) Martens, M.; Schlegel, J.; Vogt, P.; Brunner, F.; Lossy, R.; Würfl, J.; Weyers, M.; Kneissl, M. High Gain Ultraviolet Photodetectors based on AlGaN/GaN Heterostructures for Optical Switching. *Appl. Phys. Lett.* **2011,** *98* (21), 211114.

(12) Satterthwaite, P. F.; Yalamarthy, A. S.; Scandrette, N. A.; Newaz, A.; Senesky, D. G. High Responsivity, Low Dark Current Ultraviolet Photodetectors based on Two-Dimensional Electron Gas interdigitated Transducers. *ACS Photonics* **2018,** *5* (11), 4277-4282.

(13) Ma, Z.; Liu, D., *Inorganic Flexible Optoelectronics: Materials and Applications*. John Wiley & Sons: 2019.

(14) Ruh, D.; Reith, P.; Sherman, S.; Theodor, M.; Ruhhammer, J.; Seifert, A.; Zappe, H., Stretchable Optoelectronic Circuits Embedded in a Polymer Network. *Adv. Mater.* **2014,** *26* (11), 1706-1710.

(15) Russew, M. M.; Hecht, S., Photoswitches: from Molecules to Materials. *Adv. Mater.* **2010,** *22* (31), 3348-3360.

(16) Rogers, J. A.; Someya, T.; Huang, Y., Materials and Mechanics for Stretchable Electronics. *Science* **2010,** *327* (5973), 1603-1607.

(17) Kim, M.; Seo, J.-H.; Singisetti, U.; Ma, Z., Recent Advances in Free-Standing Single Crystalline Wide Band-gap Semiconductors and their Applications: GaN, SiC, ZnO, β-Ga_2O_3, and Diamond. *J. Mater. Chem. C* **2017,** *5* (33), 8338-8354.

(18) Seo, J.-H.; Swinnich, E.; Zhang, Y.-Y.; Kim, M., Low Dimensional Freestanding Semiconductors for Flexible Optoelectronics: Materials, Synthesis, Process, and Applications. *Mater. Res. Lett.* **2020,** *8* (4), 123-144.

(19) Mhedhbi, S.; Lesecq, M.; Altuntas, P.; Defrance, N.; Cordier, Y.; Damilano, B.; Jimenez, G. T.; Ebongue, A.; Hoel, V., Recent improvement of flexible GaN-based HEMT technology. *Phys. Status Solidi A* **2017,** *214* (4), 1600484.

(20) Chu, C.-F.; Lai, F.-I.; Chu, J.-T.; Yu, C.-C.; Lin, C.-F.; Kuo, H.-C.; Wang, S. Study of GaN Light-emitting Diodes Fabricated by Laser Lift-off Technique. *J. Appl. Phys.* **2004,** *95* (8), 3916-3922.

(21) Park, S. H.; Yuan, G.; Chen, D.; Xiong, K.; Song, J.; Leung, B.; Han, J. Wide Bandgap III-Nitride Nanomembranes for Optoelectronic Applications. *Nano Lett.* **2014,** *14* (8), 4293-4298.

(22) Glavin, N. R.; Chabak, K. D.; Heller, E. R.; Moore, E. A.; Prusnick, T. A.; Maruyama, B.; Walker Jr, D. E.; Dorsey, D. L.; Paduano, Q.; Snure, M. Flexible Gallium Nitride for High-Performance, Strainable Radio-Frequency Devices. *Adv. Mater.* **2017,** *29* (47), 1701838.

(23) Seo, J.-H.; Li, J.; Lee, J.; Gong, S.; Lin, J.; Jiang, H.; Ma, Z., A Simplified Method of making Flexible Blue LEDs on a Plastic Substrate. *IEEE Photonics J.* **2015,** *7* (2), 1-7.

(24) Kim, M.; Seo, J.-H.; Yu, Z.; Zhou, W.; Ma, Z. Flexible Germanium Nanomembrane Metal-Semiconductor-Metal Photodiodes. *Appl. Phys. Lett.* **2016,** *109* (5), 051105.

(25) Kim, M.; Seo, J.-H.; Zhao, D.; Liu, S.-C.; Kim, K.; Lim, K.; Zhou, W.; Waks, E.; Ma, Z. Transferrable Single Crystalline 4H-SiC Nanomembranes. *J. Mater. Chem. C* **2017,** *5* (2), 264-268.

(26) Kim, D.-H.; Ahn, J.-H.; Choi, W. M.; Kim, H.-S.; Kim, T.-H.; Song, J.; Huang, Y. Y.; Liu, Z.; Lu, C.; Rogers, J. A. Stretchable and Foldable Silicon Integrated Circuits. *Scinece* **2008,** *320* (5875), 507-511.

(27) Lee, H.; Perozek, J.; Bayram, C. In *Scaling AlGaN/GaN High Electron Mobility Transistor Structures onto 200-mm Silicon (111) Substrates through Novel Buffer Layer Configurations*, 2017 International Conference on Compound Semiconductor Manufacturing Technology, 2017.

(28) Manuel, J. M.; Morales, F. M.; Carcia, R.; Aidam, R.; Kirste, L.; Ambacher, O. Threading Dislocation Propagation in AlGaN/GaN based HEMT Structures Grown on Si (111) by Plasma Assisted Molecular Beam Epitaxy. *J. Cryst. Growth* **2012**, 357, 35-41.

(29) Chierchia, R.; Bottcher, T.; Heinke, H.; Einfeldt, S.; Figge, S.; Hommel, D. Microstructure of Heteroepitaxial GaN revealed by X-Ray Diffraction. *J. Appl. Phys.* **2003**, 93 (11), 8918-8925.

(30) Hwang, Y.; Ahn, S.; Dong, C.; Zhu, W.; Kim, B.; Le, L.; Ren, F. Lind, A. G.; Dahl, J.; Jones, K. S.; Pearton, S. J.; Kravchenko, I. I.; Zhang, M. Degradation mechanisms of Ti/Al/Ni/Au-based Ohmic contacts on AlGaN/GaN HEMTs. *J. Vac. Sci. Technol. B* **2015**, 33(3), 031212.

(31) Cui, J.; Xiao, H.; Cao, D.; Ji, Z.; Ma, J. Porosity-induced Relaxation of Strains at different Depth of Nanoporous GaN studied using the Z-scan of Raman Spectroscopy. *J. Alloys Compd.* **2015,** *626*, 154-157.

(32) Hsu, S.; Pong, B.; Li, W.; Beechem III, T. E.; Graham, S.; Liu, C. Stress Relaxation in GaN by Transfer Bonding on Si Substrates. *Appl. Phys. Lett.* **2007,** *91* (25), 251114.

(33) Garg, M.; Tak, B. R.; Rao, V. R.; Singh, R. Enhanced Performance of MSM UV Photodetectors by Molecular Modification of Gallium Nitride Using Porphyrin Organic Molecules. *IEEE Trans. Electron Devices* **2019,** *66* (4), 2036-2039.

(34) Zhang, Y.; Qian, L.; Lai, P.; Dai, T.; Liu, X. Improved Detectivity of Flexible a-InGaZnO UV Photodetector via Surface Fluorine Plasma Treatment. *IEEE Trans. Electron Devices* **2019,** *40* (10), 1646-1649.

(35) Mukherjee, B.; Cai, Y.; Tan, H. R.; Feng, Y. P.; Tok, E. S.; Sow, C. H. NIR Schottky Photodetectors based on Individual Single-Crystalline GeSe Nanosheet. *ACS Appl. Mater. Interfaces* **2013,** *5* (19), 9594-9604.

(36) Garg, M.; Tak, B. R.; Rao, V. R.; Singh, R. Giant UV Photoresponse of GaN-based Photodetectors by Surface Modification using Phenol-Functionalized Porphyrin Organic Molecules. *ACS Appl. Mater. Interfaces* **2019,** *11* (12), 12017-12026.

(37) An, Y.; Behnam, A.; Pop, E.; Ural, A. Metal-Semiconductor-Metal Photodetectors based on Graphene/p-type Silicon Schottky Junctions. *Appl. Phys. Lett.* **2013,** *102* (1), 013110.

(38) Xu, G.; Salvador, A.; Kim, W.; Fan, Z.; Lu, C.; Tang, H.; Morkoç, H.; Smith, G.; Estes, M.; Goldenberg, B. High Speed, Low Noise Ultraviolet Photodetectors based on GaN pin and AlGaN (p)-GaN (i)-GaN (n) Structures. *Appl. Phys. Lett.* **1997,** *71* (15), 2154-2156.

(39) Kumar, S.; Pratiyush, A. S.; Dolmanan, S. B.; Tripathy, S.; Muralidharan, R.; Nath, D. N. UV Detector based on InAlN/GaN-on-Si HEMT Stack with Photo-to-Dark Current Ratio > 10^7. *Appl. Phys. Lett.* **2017,** *111* (25), 251103.

(40) Arslan, E.; Bütün, S.; Lisesivdin, S. B.; Kasap, M.; Ozcelik, S.; Ozbay, E. The Persistent Photoconductivity Effect in AlGaN/GaN Heterostructures grown on Sapphire and SiC Substrates. *J. Appl. Phys.* **2008,** *103* (10), 103701.

(41) Peng, M.; Liu, Y.; Yu, A.; Zhang, Y.; Liu, C.; Liu, J.; Wu, W.; Zhang, K.; Shi, X.; Kou, J. Flexible Self-Powered GaN Ultraviolet Photoswitch with Piezo-Phototronic Effect enhanced On/Off Ratio. *ACS Nano* **2016,** *10* (1), 1572-1579.

(42) Weng, W.-Y.; Hsueh, T.-J.; Chang, S.-J.; Wang, S.-B.; Hsueh, H.-T.; Huang, G.-J. A High-Responsivity GaN Nanowire UV Photodetector. *IEEE J. Sel. Top. Quantum Electron.* **2010,** *17* (4), 996-1001.

(43) Zhang, W.; Jiang, D.; Zhao, M.; Duan, Y.; Zhou, X.; Yang, X.; Shan, C.; Qin, J.; Gao, S.; Liang, Q. Piezo-Phototronic Effect for Enhanced Sensitivity and Response Range of ZnO Thin Film Flexible UV Photodetectors. *J. Appl. Phys.* **2019,** *125* (2), 024502.

(44) Núñez, C. G.; Vilouras, A.; Navaraj, W. T.; Liu, F.; Dahiya, R. ZnO Nanowires-based Flexible UV Photodetector System for Wearable Dosimetry. *Sens. J.* **2018,** *18* (19), 7881-7888.

(45) Tak, B. R.; Gupta, V.; Kapoor, A. K.; Chu, Y.-H.; Singh, R. Wearable Gallium Oxide Solar-Blind Photodetectors on Muscovite Mica Having Ultrahigh Photoresponsivity and Detectivity with Added High-Temperature Functionalities. *ACS Appl. Electron. Mater.* **2019,** *1* (11), 2463-2470.

(46) Velusamy, D. B.; Haque, M. A.; Parida, M. R.; Zhang, F.; Wu, T.; Mohammed, O. F.; Alshareef, H. N. 2D Organic–Inorganic Hybrid Thin Films for Flexible UV–Visible Photodetectors. *Adv. Funct. Mater.* **2017,** *27* (15), 1605554.

(47) Zhang, T.; Wang, F.; Zhang, P.; Wang, Y.; Chen, H.; Li, J.; Wu, J.; Chen, L.; Chen, Z. D.; Li, S. Low-Temperature Processed Inorganic Perovskites for Flexible Detectors with a Broadband Photoresponse. *Nanoscale* **2019,** *11* (6), 2871-2877.

(48) Mahdi, M. S.; Ibrahim, K.; Hmood, A.; Ahmed, N. M.; Azzez, S. A.; Mustafa, F. I. A Highly Sensitive Flexible SnS Thin Film Photodetector in the Ultraviolet to Near Infrared prepared by Chemical Bath Deposition. *RSC Adv.* **2016,** *6* (116), 114980-114988.

(49) Ambacher, O.; Foutz, B.; Smart, J.; Shealy, J. R.; Weimann, N. G.; Chu, K.; Murphy, M.; Sierakowski, A. J.; Schaff, W. J.; Eastman, L. F. Two Dimensional Electron Gases Induced by Spontaneous and Piezoelectric Polarization in Undoped and Doped AlGaN/GaN Heterostructures. *J. Appl. Phys.* **2000**, 87 (1), 334-343.

(50) Pal, J.; Tse, G.; Haxha, V.; Migliorato, M. A.; Tomić, S. Second-Order Piezoelectricity in Wurtzite III-N Semiconductors. *Phys. Rev. B* **2011,** *84* (8), 085211.